Delineation of Human Carotid Plaque Features *In Vivo* by Exploiting Displacement Variance

Gabriela Torres, *Student Member, IEEE*, Tomasz J. Czernuszewicz, Jonathon W. Homeister, Melissa C. Caughey, Benjamin Y. Huang, Ellie R. Lee, Carlos A. Zamora, Mark A. Farber, William A. Marston, David Y. Huang, Timothy C. Nichols, and Caterina M. Gallippi, *Member, IEEE*

***Abstract*— While *in vivo* acoustic radiation force impulse (ARFI)-induced peak displacement (PD) has been demonstrated to have high sensitivity and specificity for differentiating soft from stiff plaque components in patients with carotid plaque, the parameter exhibits poorer performance for distinguishing between plaque features with similar stiffness. To improve discrimination of carotid plaque features relative to PD, we hypothesize that signal correlation and signal-to-noise ratio (SNR) can be combined, outright or via displacement variance. Plaque feature detection by displacement variance, evaluated as the decadic logarithm of the variance of acceleration and termed "log(VoA)," was compared to that achieved by exploiting SNR, cross correlation coefficient, and ARFI-induced PD outcome metrics. Parametric images were rendered for 25 patients undergoing carotid endarterectomy, with spatially matched histology confirming plaque composition and structure. On average, across all plaques, log(VoA) was the only outcome metric with values that statistically differed between regions of lipid-rich necrotic core (LRNC), intraplaque hemorrhage (IPH), collagen (COL), and calcium (CAL). Further, log(VoA) achieved the highest contrast-to-noise ratio (CNR) for discriminating between LRNC and IPH, COL and CAL, and grouped soft (LRNC and IPH) and stiff (COL and CAL) plaque components. More specifically, relative to the previously demonstrated ARFI PD parameter, log(VoA) achieved 73% higher CNR between LRNC and IPH and 59% higher CNR between COL and CAL. These results suggest that log(VoA) enhances the differentiation of LRNC, IPH, COL, and CAL in human carotid plaques, *in vivo*, which is clinically relevant to improving stroke risk prediction and medical management.**

***Index Terms*— Acoustic radiation force impulse (ARFI) imaging, atherosclerosis, carotid endarterectomy (CEA), carotid plaque characterization.**

Manuscript received December 19, 2018; accepted February 4, 2019. Date of publication February 11, 2019; date of current version March 14, 2019. This work was supported by the NIH under Grant R01HL092944, Grant R01NS074057, Grant R01DK107740, Grant T32HL069768, and Grant K02HL105659. *(Corresponding author: Caterina M. Gallippi.)*

G. Torres and C. M. Gallippi are with the Joint Department of Biomedical Engineering, University of North Carolina at Chapel Hill, Chapel Hill, NC 27514 USA, and North Carolina State University, Raleigh, NC 27695 USA (e-mail: cmgallip@email.unc.edu).

T. J. Czernuszewicz was with the Joint Department of Biomedical Engineering, University of North Carolina at Chapel Hill, Chapel Hill, NC 27514 USA, and North Carolina State University, Raleigh, NC 27695 USA. He is now with SonoVol, Inc., Durham, NC USA.

J. W. Homeister is with the Department of Pathology and Laboratory Medicine, University of North Carolina at Chapel Hill, Chapel Hill, NC USA.

M. C. Caughey is with the Department of Medicine, University of North Carolina at Chapel Hill, Chapel Hill, NC USA.

B. Y. Huang, E. R. Lee, and C. A. Zamora are with the Department of Radiology, University of North Carolina at Chapel Hill, Chapel Hill, NC USA.

M. A. Farber and W. A. Marston are with the Department of Surgery, University of North Carolina at Chapel Hill, Chapel Hill, NC USA.

D. Y. Huang is with the Department of Neurology, University of North Carolina at Chapel Hill, Chapel Hill, NC USA.

T. C. Nichols is with the Department of Pathology and Laboratory Medicine, University of North Carolina at Chapel Hill, Chapel Hill, NC, USA, and also with the Department of Medicine, University of North Carolina at Chapel Hill, Chapel Hill, NC USA.

Digital Object Identifier 10.1109/TUFFC.2019.2898628

I. Introduction

ATHEROSCLEROSIS ranks among the leading causes of cardiovascular death in the United States [1]. The disease progresses slowly and can remain asymptomatic until very late stages, making it difficult to identify and treat. Furthermore, atherosclerotic lesions may or may not develop into what are considered "vulnerable plaques," a term associated with those plaques at greatest risk for rupture and subsequent ischemic events. Vulnerable plaques are frequently not the largest or the most obstructive; instead, their relative risk is governed by their composition and structure [2]–[5]. A number of compositional and structural elements distinguish a vulnerable plaque, including a thin or ruptured fibrous cap, a large lipid-rich necrotic core (LRNC), and intraplaque hemorrhage (IPH). Thus, an imaging method that reliably identifies these plaque features would facilitate medical management of patients with atherosclerosis.

Typically, minimally invasive imaging techniques, such as conventional angiography, as well as noninvasive imaging approaches, such as ultrasound carotid intima-media thickness and Doppler flow measurements, have been used to detect atherosclerotic plaque [6]–[10]. These techniques, however, can give false negatives in arteries that have undergone vascular remodeling [11], and they are incapable of characterizing the material and structural composition of the plaque [12], [13].

Plaque composition has been interrogated noninvasively by imaging methods that exploit tissue mechanical properties. For example, in ultrasound strain imaging, tissue displacement in response to physiological pulsation is used to identify regions of high strain that correspond to atheromatous material. Hansen *et al.* [14], [15] implemented compound ultrasound strain imaging (CUSI) to differentiate fibro-atheromatous carotid plaque in humans, *in vivo*. Roy-Cardinal *et al.* [16] combined strain elastography, homodyned-K parametric maps,

and B-mode gray levels to detect small lipid areas and large calcifications in patients with carotid plaque, *in vivo*. Wang *et al.* [17] distinguished between symptomatic and asymptomatic carotid plaque patients by developing biomarkers based on plaque strain indices. Nayak *et al.* [18] reported that principal strain elastography improved reliability of arterial strain estimations independently of the transducer angle. Li *et al.* [19] described pulse wave imaging coupled with strain imaging for differentiating carotid plaque calcification stages in a pilot clinical study.

In addition to strain imaging, acoustic radiation force (ARF)-based elasticity imaging methods have been proposed for plaque characterization [20]–[29]. ARF-based elasticity imaging techniques use ultrasound energy to induce a stress in tissue that creates a measurable deformation, and the induced deformation is assessed to infer the underlying tissue mechanical properties. For example, in ARF impulse (ARFI) ultrasound, an ARFI is delivered to a specific region of excitation, and the induced dynamic displacements within the region of excitation are monitored over time to reflect tissue stiffness [30].

Previous ARFI imaging studies conducted by our group and others have shown that atherosclerotic plaque characterization by ARFI is feasible [22], [24], [26]. More specifically, our previous *ex vivo* and *in vivo* studies involving spatially matched histological validation of ARFI imaging results [31], [32] demonstrated that collagen (COL), calcium (CAL) deposits, and fibrous caps correlated with areas of relatively low ARFI-induced peak displacement (PD), consistent with the expected response of stiff materials. Further, LRNC and IPH correlated with areas of relatively high PD, consistent with the expected response of soft materials. Using a statistical reader study including three trained, blinded radiologists, we calculated the area under the receiver operating curve (AUROC) of ARFI PD for delineating plaque components in human carotid arteries *in vivo* [33]. The results revealed that while PD effectively detected soft (median AUROC $= 0.887$) and stiff (median AUROC $= 0.859$) plaque features, PD was not as successful at distinguishing between different plaque components that exhibited similar PDs (median AUROCs < 0.65).

Inability to distinguish between soft LRNC and IPH features impairs ARFI's clinical relevance to atherosclerosis imaging because LRNC has lower hazard ratio (3) than IPH (4.59) in regard to predicting subsequent stroke/transient ischemic attack [34]. Thus, differentiating IPH from LRNC could improve identification of patients in need of invasive interventions, such as a carotid endarterectomy (CEA), to prevent stroke versus those that could safely be managed pharmaceutically [34]. Similarly, inability to distinguish between stiff COL and CAL diminishes ARFI's utility for atherosclerosis imaging because diffuse COL deposition is generally considered stabilizing to plaques, while CAL deposits may be stabilizing or destabilizing depending on their size and location [35]. Thus, knowledge that a stiff region in a carotid plaque is COL as opposed to CAL could improve stroke risk assessment and facilitate medical management.

The purpose of this study was to determine if plaque features that exhibit similar ARFI PDs are better discriminated by alternative ARFI-derived outcome parameters. These parameters exploit signal correlation and signal-to-noise ratio (SNR), which vary between plaque components according to displacement and echogenicity, respectively. Thus, relative to evaluating PD alone, evaluating signal correlation could improve discrimination of plaque features by mechanical property. Further, evaluating SNR enables discrimination of plaque features by echogenic property. In addition to outright signal correlation and SNR, we evaluate if displacement estimation variance, which is a function of both correlation and SNR, improves discrimination of plaque features. We hypothesize that signal correlation and SNR can be exploited, outright or via displacement variance, to improve discrimination of carotid plaque features relative to PD in transcutaneous ARFI imaging. We performed this work by deriving correlation, SNR, and displacement variance parameters from the same ARFI data previously acquired *in vivo* from the carotid plaques of 25 patients undergoing clinically indicated CEA [33].

II. Methods

As described above, all analyses were applied to previously collected *in vivo* human carotid plaque data, the acquisition and nature of which have been described in detail previously [33]. Briefly, 25 patients undergoing clinically indicated CEA were recruited from UNC Hospitals. The University of North Carolina Chapel Hill Institutional Review Board approved all procedures in this study. Informed consent was given from each study participant (ClinicalTrials.gov No. NCT01581385). From the 25 patients, five plaques met the exclusion criteria outlined in [33] and were not considered.

The examined plaques were imaged *in vivo* prior to surgery using a Siemens Acuson Antares (Siemens Medical Solutions USA Inc., Ultrasound Division, Issaquah, WA, USA) and a VF7-3 linear array, and the CEA specimens were collected following surgery for histological validation of imaging results. The extracted plaque specimens were imaged with volumetric micro-CT. Micro-CT volumes were segmented into CAL and soft tissue, and were aligned with morphology on the B-mode frame (acquired simultaneously with ARFI data) to identify the proper sectioning plane to achieve spatial alignment of ARFI and histology data. Sections were stained with hematoxylin and eosin (H&E), Von Kossa (VK) for CAL, and combined Masson's elastin (CME) for COL. Fig. 1 provides a flowchart of this procedure from an example carotid plaque in a 71-year-old symptomatic male. The histology images were read by a pathologist (Homeister) experienced in atherosclerosis, who marked regions of COL, CAL, LRNC, and IPH. The reader is referred to our prior publication for more detailed descriptions of the study population, ultrasound data acquisition, and histological processing methods.

A. Outcome Parameter Estimation

Outcome parameters were systematically generated, as indicated in Fig. 2, for three input data sources: 1) ARFI-induced displacement; 2) cross correlation coefficient (CC); and

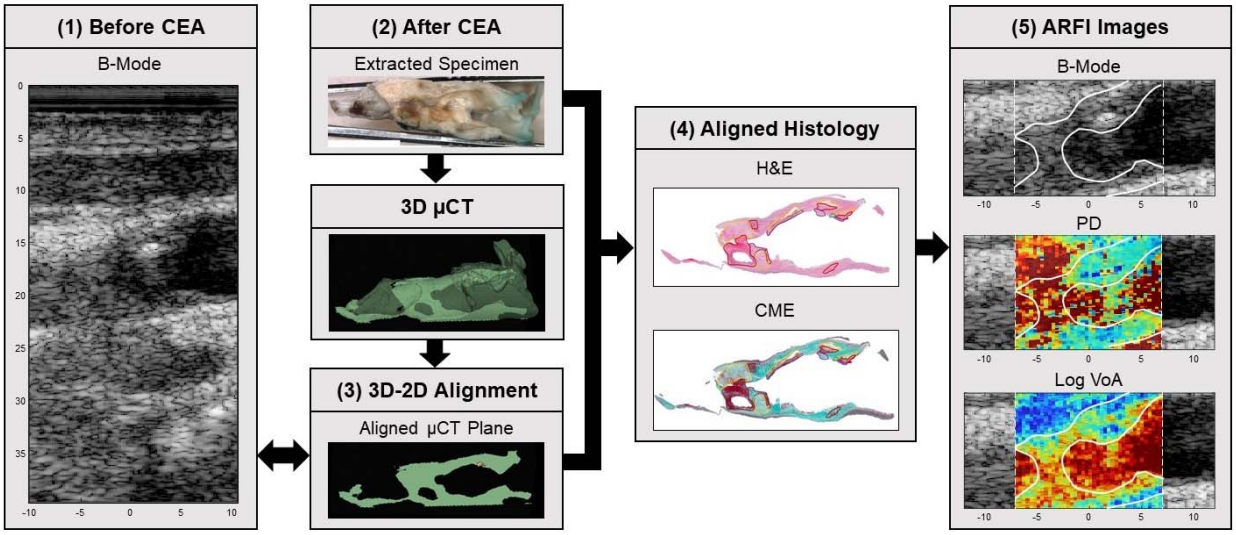

Fig. 1. Procedure for aligning histology and ARFI images. (1) First, before CEA, *in vivo* B-mode (and matched ARFI) data are recorded from the plaque. (2) After CEA, a μCT volume of the extracted specimen is rendered. (3) Using anatomy and morphology in the B-mode image, an aligned plane is located along the μCT volume. (4) This aligned μCT is used to identify the plane for sectioning the specimen during histological processing such that the histology and ultrasound imaging planes are aligned. (5) Finally, features identified by the pathologist on the spatially aligned histology slides are used as validation for parametric ultrasound image analysis. The depicted carotid plaque example is from a 71-year-old symptomatic male.

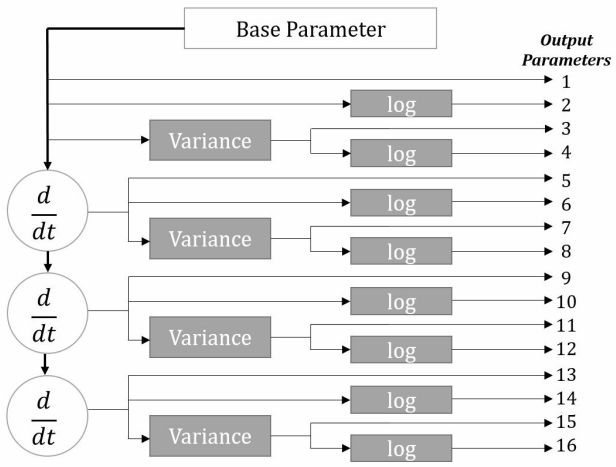

Fig. 2. Flowchart of the systematic parameter evaluation, where there is a base data set (ARFI displacement, RF SNR, or CC) as an input, and 16 output parameters per base data set.

3) radio frequency SNR. All three data sources were evaluated over ensemble time. ARFI-induced displacement and CC were calculated using normalized 1-D axial cross correlation with a kernel length of 1.5λ [36]. Note that the selection of this kernel length is based on a previous study [37] that evaluated the tradeoff between bias in plaque feature size estimates with large kernel sizes and noise in displacement estimates with small kernel sizes. Radio frequency SNR was calculated as μ/σ, where μ represents the signal amplitude in each independent pixel per frame, and σ represents the noise component, which was calculated as the average signal amplitude in a 3×3 mm^2 anechoic region inside the lumen of each carotid artery. The size of the noise region was selected as the size of the largest anechoic region consistently recognizable in all of the carotid images. The three sources of input data were each evaluated in terms of the nth time derivate (with $n = 0$, 1, 2, and 3), the decadic logarithm of the nth time derivate, the temporal variance of the nth time derivate, and the decadic logarithm of the temporal variance of the nth time derivate.

To understand the motivation for taking the time derivative, consider that this operation is a high-pass filter that accentuates variance in the input data source. When the input data source is displacement, variance in the estimate, also known as "jitter," is predicted using the Cramer–Rao lower bound [38] as

$$\sigma \geq \sqrt{\frac{3}{2f^3\pi^2 T(B^3+12B)}\left[\frac{1}{CC^2}\left(1+\frac{1}{\mathrm{SNR}^2}\right)^2-1\right]} \quad (1)$$

where f is the center frequency, T is the tracking kernel size, and B is the bandwidth. If these three parameters are maintained constant, jitter magnitude is primarily a function of CC and SNR. Thus, by evaluating the time derivative(s) of displacement, signal components with different degrees of decorrelation and/or SNR level may be differentiated. On the contrary, considering CC or SNR alone differentiates signal components on the basis of only the single corresponding parameter. For all three input data sources, temporal (unbiased) variance was calculated as

$$V_p(x,y,t_i)=\frac{1}{k-1}\sum_{j=i}^{i+(k-1)}\left|p(x,y,t_j)-\frac{1}{k}\sum_{l=i}^{i+(k-1)}p(x,y,t_l)\right|^2 \quad (2)$$

where p is the input data source, x and y are the axial and lateral coordinates, respectively, and t is time. The window length for the variance calculation k was five time samples (corresponding to 0.5 ms for the employed pulse repetition frequency of 10 kHz). Using these operations, a total of 16 output parameters were generated for each input data source, for a total of 16 output parameters/input data source $\times 3$ input data sources $= 48$ output parameters.

B. Image Rendering and Performance Analysis

For the *in vivo* human carotid plaque examples, parametric images of the 48 outcome parameters were rendered by displaying the median parameter value over the last two milliseconds of ensemble time for each pixel. For display and analysis purposes, all parametric images were normalized to the median value within the plaque +/− two mean absolute deviations.

From the parametric images, plaque components (COL, CAL, LRNC, and IPH) were segmented using a semiautomatic k-means clustering method [39]. First, aligned histology and parametric images were cropped to span the ultrasonically interrogated plaque region. Then, from the cropped histology image, the centroids of the plaque features identified by the pathologist were calculated. Next, by resizing the image using bicubic interpolation (MATLAB, Mathworks Inc., Natick, MA, USA), the number of lateral and axial pixels in the cropped histology image was matched to the number of lateral and axial pixels in the cropped parametric image. Finally, the centroid positions after resizing were input to the k-means algorithm as the starting locations for k regions to be segmented in the parametric image, where k is the number of plaque component regions identified by the pathologist.

For the segmented plaque features across all plaques, the values of each outcome parameter were statistically compared between plaque features using pairwise Wilcoxon rank sum tests with significance levels of 0.01 and 0.05. In addition, feature contrast-to-noise ratio (CNR) was computed as

$$\mathrm{CNR} = \frac{|\mu_f - \mu_b|}{\sqrt{\sigma_f^2 + \sigma_b^2}} \tag{3}$$

where μ and σ are the mean and standard deviation within the segmented region, and the subscripts f and b refer to the feature and background regions, respectively. For the purposes of this study, IPH was a "feature" evaluated relative to LRNC "background," CAL was a "feature" evaluated relative to COL "background," and grouped soft plaque elements (LRNC and IPH) were a "feature" evaluated relative to grouped "stiff" plaque elements (CAL and COL) as the "background." In addition, CNR coefficient of variation (CV) was calculated as $\sigma_{\mathrm{CNR}}/\mu_{\mathrm{CNR}}$.

III. Results

Figs. 3–5 show the 16 displacement-, SNR-, and CC-based parametric images, respectively, of an American Heart Association Type VI plaque [2] in the carotid artery of a symptomatic 53-year-old female. In Fig. 3, the time-derivative operation accentuates high-frequency jitter in the ARFI displacement profiles. Then, the accentuated jitter content is exploited using the variance calculation. The logarithmic representation of these results expands the dynamic range and improves contrast. Note that the first time derivative of displacement is referred to as "velocity," the second time derivative as "acceleration," and the third time derivative as "jerk." The variance of the parameter is denoted as "Vo," and the decadic log is denoted as "log," such that log(VoA) is the decadic log of the variance of the second time derivative of displacement.

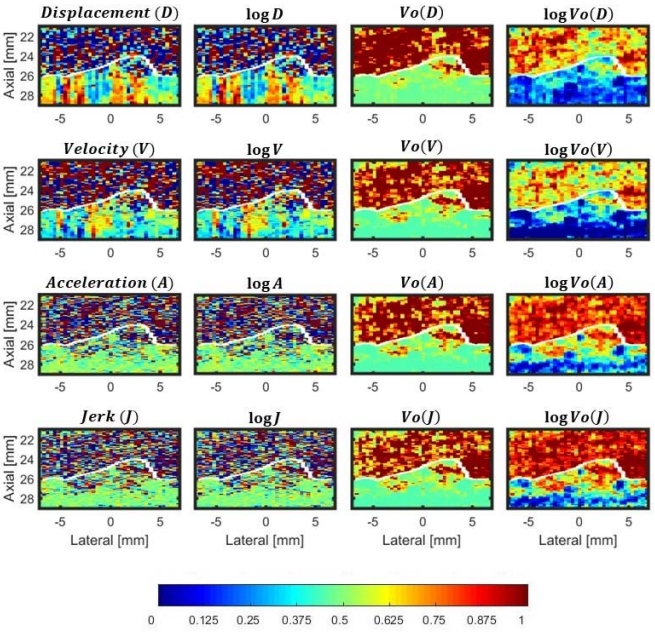

Fig. 3. Parametric images of a carotid plaque from a 53-year-old symptomatic female. Base parameter: ARFI displacement. V_0 indicates variance calculation; *log* indicates decadic logarithm.

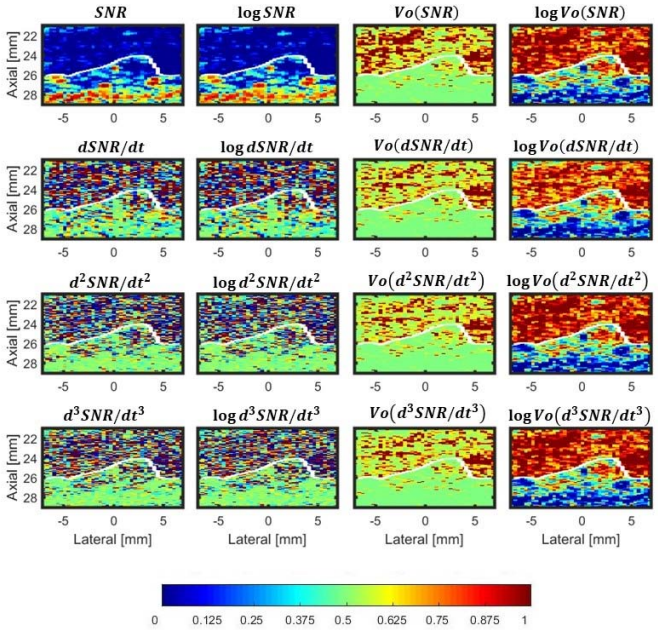

Fig. 4. Parametric images of a carotid plaque from a 53-year-old symptomatic female. Base parameter: SNR. $d^n\mathrm{SNR}/dt^n$ indicates the nth time derivative; V_0 indicates variance calculation; *log* indicates decadic logarithm.

Figs. 6–8 show distributions of outcome parameter values by plaque feature for all examined carotid plaques, as derived from ARFI displacement, SNR, and CC, respectively. Features with parameter distributions that statistically differ from each other ($p < 0.01$ or $p < 0.05$) are indicated by a black bar and asterisk or blue bar and circle, respectively, below the graph. From this analysis, the only parameter with statistically different distributions between CAL and COL, between COL and LRNC, and between LRNC and IPH was log(VoA). This parameter achieved the following normalized ranges for each

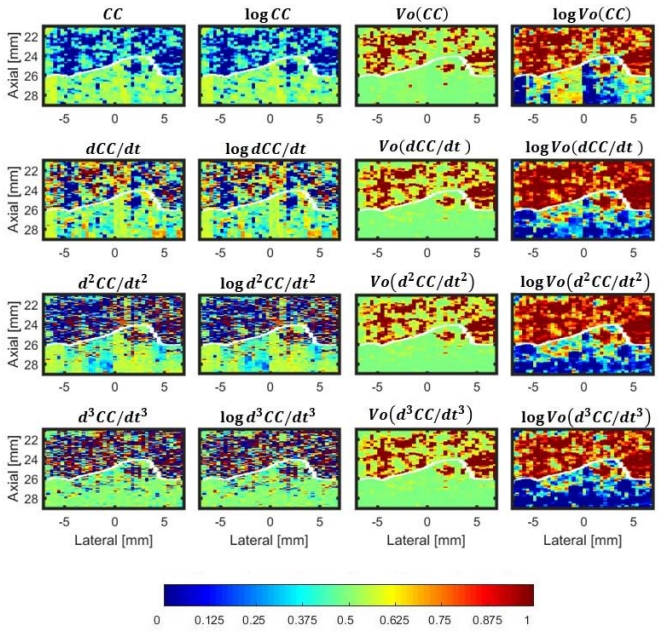

Fig. 5. Parametric images of a carotid plaque from a 53-year-old symptomatic female. Base parameter: CC. $d^n\mathrm{CC}/dt^n$ indicates the nth time derivative; V_0 indicates variance calculation; *log* indicates decadic logarithm.

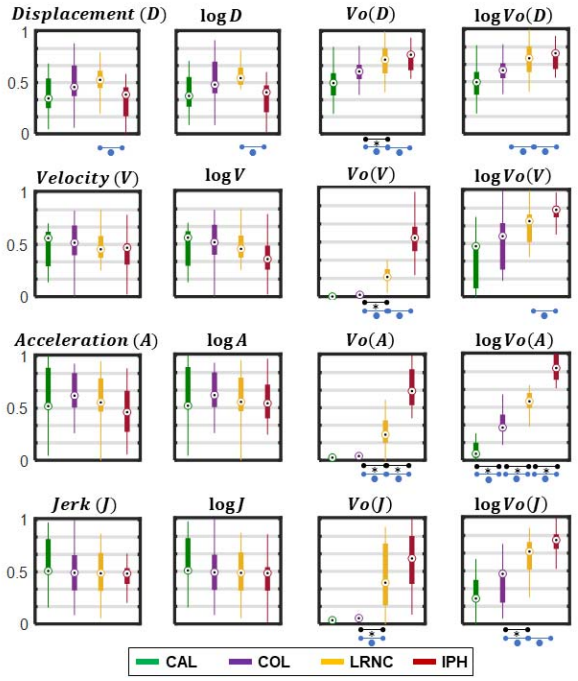

Fig. 6. Normalized parameter value distributions by plaque feature for 20 carotid plaque examples. Distributions that are statistically different with $p < 0.01$ are indicated with a black asterisk, while distributions with $p < 0.05$ are indicated with a blue circle. Base parameter: ARFI displacement. V_0 indicates variance calculation; *log* indicates decadic logarithm.

component, expressed as median [$Q1$, $Q3$], where $Q1$ and $Q3$ are the 25th and 75th percentile values, respectively: IPH: 0.87 [0.76, 1.00], LRNC: 0.56 [0.49, 0.63], COL: 0.31 [0.27, 0.43], CAL: 0.06 [0.02, 0.17].

In addition, feature CNR by parameter is indicated in Tables I–III for ARFI displacement, SNR, and CC, respectively. The highest CNR value for each input data source

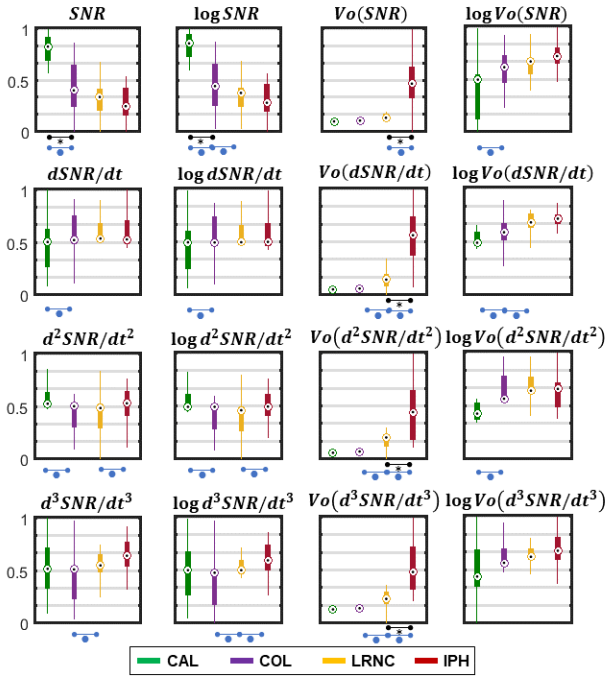

Fig. 7. Normalized parameter value distributions by plaque feature for 20 carotid plaque examples. Distributions that are statistically different with $p < 0.01$ are indicated with a black asterisk, while distributions with $p < 0.05$ are indicated in blue. Base parameter: SNR. $d^n\mathrm{SNR}/dt^n$ indicates the nth time derivative; V_0 indicates variance calculation; *log* indicates decadic logarithm.

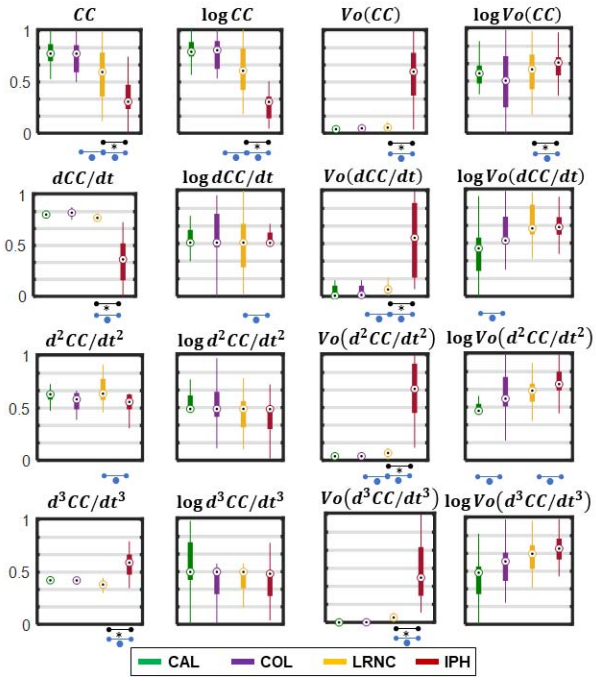

Fig. 8. Normalized parameter value distributions by plaque feature for 20 carotid plaque examples. Distributions that are statistically different with $p < 0.01$ are indicated with a black asterisk, while distributions with $p < 0.05$ are indicated in blue. Base parameter: CC. $d^n\mathrm{CC}/dt^n$ indicates the nth time derivative; V_0 indicates variance calculation; *log* indicates decadic logarithm.

is shown in green, and the second highest is shown in yellow. CNR CV is indicated parenthetically. The three best performing parameters were decadic logarithm of the variance of acceleration [log(VoA)], log(SNR), and Vo(dCC/dt).

TABLE I

PLAQUE FEATURE CNR FOR ARFI DISPLACEMENT-DERIVED PARAMETERS. CNR COEFFICIENTS OF VARIATION ARE INDICATED BETWEEN PARENTHESES. V_0 INDICATES VARIANCE CALCULATION; *log* INDICATES DECADIC LOGARITHM

Feature Differentiation	CNR							
	$Displacement\ (D)$	$\log D$	$Vo(D)$	$\log Vo(D)$	$Velocity\ (V)$	$\log V$	$Vo(V)$	$\log Vo(V)$
LRNC v. IPH	0.90 (0.89)	0.91 (0.88)	1.12 (0.74)	0.88 (0.85)	0.77 (0.84)	0.82 (0.93)	1.13 (0.81)	**1.14** (0.73)
COL v. CAL	0.76 (0.79)	0.77 (0.80)	1.54 (0.64)	0.74 (0.94)	0.88 (0.55)	0.88 (0.55)	**2.12** (0.46)	0.93 (0.42)
COL v. LRNC	0.62 (1.14)	0.62 (1.16)	**1.54** (0.63)	0.82 (0.92)	0.82 (0.56)	0.82 (0.56)	1.44 (0.65)	1.25 (0.49)
Soft v. Stiff	0.85 (0.84)	0.85 (0.84)	2.61 (0.37)	1.18 (0.40)	0.86 (0.62)	0.79 (0.80)	**3.02** (0.32)	2.27 (0.35)
	$Acceleration\ (A)$	$\log A$	$Vo(A)$	$\log Vo(A)$	$Jerk\ (J)$	$\log J$	$Vo(J)$	$\log Vo(J)$
LRNC v. IPH	0.69 (0.91)	0.89 (0.80)	0.75 (0.70)	**1.45** (0.61)	0.71 (1.15)	0.50 (1.22)	0.85 (0.71)	0.97 (0.85)
COL v. CAL	0.83 (0.87)	0.83 (0.87)	1.13 (0.55)	**2.30** (0.42)	0.37 (1.57)	0.37 (1.57)	2.03 (0.48)	0.93 (0.74)
COL v. LRNC	0.91 (0.75)	0.91 (0.75)	0.85 (1.29)	**2.07** (0.49)	0.61 (1.04)	0.61 (1.04)	1.25 (0.76)	1.03 (0.57)
Soft v. Stiff	0.80 (0.98)	0.69 (0.93)	1.75 (0.47)	**3.09** (0.31)	0.79 (0.95)	0.78 (0.94)	2.24 (0.44)	2.28 (0.31)

TABLE II

PLAQUE FEATURE CNR FOR SNR-DERIVED PARAMETERS. CNR COEFFICIENTS OF VARIATION ARE INDICATED BETWEEN PARENTHESES. $d^n\mathrm{SNR}/dt^n$ INDICATES THE nTH TIME DERIVATIVE; V_0 INDICATES VARIANCE CALCULATION; *log* INDICATES DECADIC LOGARITHM

Feature Differentiation	CNR							
	SNR	$\log SNR$	$Vo(SNR)$	$\log Vo(SNR)$	$\frac{dSNR}{dt}$	$\log\frac{dSNR}{dt}$	$Vo\left(\frac{dSNR}{dt}\right)$	$\log Vo\left(\frac{dSNR}{dt}\right)$
LRNC v. IPH	0.70 (0.81)	0.71 (0.75)	0.41 (2.18)	0.60 (1.19)	0.54 (1.71)	0.53 (1.74)	0.51 (1.71)	0.59 (1.34)
COL v. CAL	1.29 (0.66)	1.35 (0.62)	1.00 (0.98)	0.76 (0.91)	0.50 (1.21)	0.49 (1.28)	0.56 (1.66)	0.66 (0.92)
COL v. LRNC	0.79 (0.74)	0.79 (0.73)	0.08 (12.27)	0.75 (0.85)	0.72 (1.15)	0.71 (1.17)	0.62 (1.39)	0.71 (0.97)
Soft v. Stiff	1.50 (0.55)	1.52 (0.54)	0.70 (1.29)	0.94 (0.76)	0.72 (1.04)	0.71 (1.08)	1.07 (0.90)	1.01 (0.66)
	$\frac{d^2SNR}{dt^2}$	$\log\frac{d^2SNR}{dt^2}$	$Vo\left(\frac{d^2SNR}{dt^2}\right)$	$\log Vo\left(\frac{d^2SNR}{dt^2}\right)$	$\frac{d^3SNR}{dt^3}$	$\log\frac{d^3SNR}{dt^3}$	$Vo\left(\frac{d^3SNR}{dt^3}\right)$	$\log Vo\left(\frac{d^3SNR}{dt^3}\right)$
LRNC v. IPH	0.65 (1.15)	0.63 (1.20)	0.61 (1.38)	0.65 (0.81)	0.71 (0.97)	0.68 (1.04)	0.53 (1.45)	0.55 (1.08)
COL v. CAL	0.69 (0.96)	0.67 (1.04)	0.74 (1.30)	0.76 (0.77)	0.80 (1.04)	0.77 (1.10)	0.42 (2.33)	0.48 (1.10)
COL v. LRNC	0.65 (1.17)	0.64 (1.24)	0.79 (1.11)	0.67 (0.99)	0.72 (1.35)	0.70 (1.39)	0.52 (1.61)	0.46 (1.67)
Soft v. Stiff	0.89 (0.97)	0.89 (0.98)	0.70 (1.39)	1.09 (0.61)	0.69 (1.20)	0.67 (1.30)	0.54 (1.76)	0.50 (1.42)

The parameter log (VoA) yielded CNRs of 1.45 (0.61) for LRNC versus IPH, 2.30 (0.42) for COL v. CAL, 2.07 (0.49) for COL v. LRNC, and 3.09 (0.31) for soft v. stiff tissues. The parameter log(SNR) achieved CNRs of 0.71 (0.75) for LRNC v. IPH, 1.35 (0.62) for COL v. CAL, 0.79 (0.73) for COL v. LRNC, 1.52 (0.54) for soft v. stiff tissues. The parameter Vo(dCC/dt) yielded CNRs of 1.40 (0.67) for LRNC v. IPH, 0.80 (0.89) for COL v. CAL, 0.73 (0.78) for COL v. LRNC, and 1.50 (0.61) for soft v. stiff tissues. For comparison purposes, CNR values from ARFI PD were also calculated: 0.40 (0.78) for LRNC v. IPH, 0.77 (1.04) for COL v. CAL, 0.28 (0.89) for COL v. LRNC, and 1.92 (0.28) for soft v. stiff tissues. From these results, the highest CNR for all plaque features was achieved by log (VoA), followed by Vo(dCC/dt) for LRNC v. IPH, and log (SNR) for COL v. CAL. ARFI PD yielded the second highest CNR for grouped soft v. stiff tissues.

Table IV shows p-values for statistical comparisons between outcome parameter values in the specified plaque features. The outcome parameters are those with the highest overall CNR for each input data source, and PD is included for comparison purposes. The only parameter with statistically different ($p < 0.01$) distributions between all the specified features is log (VoA). In contrast, ARFI PD values in regions of LRNC and IPH were not statistically different, and neither were ARFI PD values in regions of COL and CAL. The p-value describing the likelihood that grouped soft and grouped stiff plaque features had ARFI PD values that were the same was 0.02. Consistent with CNR results, log (SNR) values in regions of COL and CAL were statistically different ($p < 0.01$), and Vo(dCC/dt) values statistically differed in regions of LRNC and IPH ($p < 0.01$).

For the same Type VI plaque of Figs. 3–5, Fig. 9 illustrates B-mode, PD, and log (VoA) images. The images are shown with and without segmented plaque components to illustrate both the raw imaging results and segmentation outputs. Histology is also shown, spatially matched to the ARFI imaging plane and stained with CME, H&E, and VK.

TABLE III

PLAQUE FEATURE CNR FOR CC-DERIVED PARAMETERS. CNR COEFFICIENTS OF VARIATION ARE INDICATED BETWEEN PARENTHESES. d^nCC/dt^n INDICATES THE nTH TIME DERIVATIVE; V_0 INDICATES VARIANCE CALCULATION; *log* INDICATES DECADIC LOGARITHM

Feature Differentiation	CNR							
	CC	$\log CC$	$Vo(CC)$	$\log Vo(CC)$	$\frac{dCC}{dt}$	$\log\frac{dCC}{dt}$	$Vo\left(\frac{dCC}{dt}\right)$	$\log Vo\left(\frac{dCC}{dt}\right)$
LRNC v. IPH	0.94 (0.73)	0.98 (0.87)	1.14 (0.83)	0.97 (0.55)	1.05 (0.91)	1.15 (0.55)	1.40 (0.67)	1.28 (0.57)
COL v. CAL	0.52 (1.02)	0.55 (0.91)	0.72 (1.09)	0.73 (1.03)	0.64 (1.08)	0.78 (0.97)	0.80 (0.89)	0.79 (1.02)
COL v. LRNC	0.64 (0.90)	0.64 (0.87)	0.58 (0.63)	0.66 (1.03)	0.70 (1.03)	0.51 (1.22)	0.73 (0.78)	0.72 (1.01)
Soft v. Stiff	1.14 (0.67)	1.14 (0.68)	1.06 (0.92)	0.89 (0.74)	1.10 (0.81)	1.15 (0.58)	1.50 (0.61)	0.91 (0.78)
	$\frac{d^2CC}{dt^2}$	$\log\frac{d^2CC}{dt^2}$	$Vo\left(\frac{d^2CC}{dt^2}\right)$	$\log Vo\left(\frac{d^2CC}{dt^2}\right)$	$\frac{d^3CC}{dt^3}$	$\log\frac{d^3CC}{dt^3}$	$Vo\left(\frac{d^3CC}{dt^3}\right)$	$\log Vo\left(\frac{d^3CC}{dt^3}\right)$
LRNC v. IPH	1.01 (0.75)	1.04 (0.71)	1.03 (0.91)	1.07 (0.61)	0.62 (1.04)	0.70 (1.10)	0.78 (1.24)	0.54 (1.29)
COL v. CAL	0.77 (0.84)	0.52 (1.20)	0.76 (0.89)	0.74 (0.70)	0.61 (1.38)	0.67 (1.25)	0.58 (1.69)	0.63 (0.83)
COL v. LRNC	0.62 (0.90)	0.69 (1.07)	0.72 (0.81)	0.69 (1.06)	0.70 (1.25)	0.65 (1.14)	0.48 (2.03)	0.64 (1.06)
Soft v. Stiff	0.74 (1.00)	0.69 (1.26)	1.05 (0.92)	1.00 (0.76)	0.59 (0.97)	0.71 (1.09)	0.89 (1.09)	0.86 (0.98)

TABLE IV

STATISTICAL SIGNIFICANCE OF THE DIFFERENCES BETWEEN LRNC AND IPH, BETWEEN COL AND CAL, AND BETWEEN GROUPED SOFT (LRNC/IPH) AND STIFF (COL/CAL) FEATURES FOR LOG(VOA)-, PD-, CC-, AND SNR-DERIVED OPTIMAL PARAMETERS. *dCC/dt* INDICATES THE FIRST TIME DERIVATIVE; V_0 INDICATES VARIANCE CALCULATION; *log* INDICATES DECADIC LOGARITHM

Feature Differentiation	CNR				N
	$\log Vo(A)$	PD	$\log SNR$	$Vo\left(\frac{dCC}{dt}\right)$	
LRNC v. IPH	**< 0.01**	0.58	0.62	**< 0.01**	14
COL v. CAL	**< 0.01**	0.19	**< 0.01**	0.31	19
COL v. LRNC	**< 0.01**	1.02	0.11	0.53	18
Soft v. Stiff	**< 0.01**	0.02	0.05	0.03	20

Pathologist markings on the histology images indicate regions of COL, CAL, LRNC, and IPH. In the PD image, CAL deposits (which are readily apparent as hyperechoic regions in the B-mode image) exhibit similar PD as regions of COL. Further, PD achieved in small regions of LRNC are not distinguishable from those measured in the surrounding COL. In addition, PDs in the region of IPH are highly relative to the other plaque regions, but it is difficult to determine if these high PDs indicate IPH or LRNC, resulting in underestimation of IPH regions. In the log (VoA) images, CAL deposits have noticeably lower log (VoA) than any other plaque features. Further, LRNC exhibits higher log (VoA) than COL. Finally, the regions of IPH have the highest overall log (VoA). These results show that by visual inspection, CAL is better distinguished from COL and IPH is better distinguished from LRNC using log (VoA) than PD.

To further demonstrate the effectiveness of log(VoA) for delineating carotid plaque components, Figs. 10 and 11 show additional examples of B-mode, PD, and log(VoA) images with spatially matched histology. In Fig. 10(b), CAL and LRNC exhibit PDs that are similar to those of COL, while IPH exhibits high PDs that could be mistaken for LRNC. In the log(VoA) image of panel (c), CAL and LRNC are distinguishable from COL, and log(VoA) values in regions of IPH are higher than those in LRNC. The segmented fibrous cap and IPH regions in the log(VoA) image more closely match the spatial distribution of these plaque components in the matched histology. In Fig. 11(b), high PD values are associated with a large region of CAL (black arrows), which is inconsistent with the expected low-displacement response of stiff CAL. These high PD values, which arise from displacement profile distortions caused by wave reflections [40], erroneously indicate a large, soft feature. While this large CAL region is mischaracterized as a soft feature in the PD image, it is appropriately indicated as a region of low log(VoA) in panel (c), consistent with the expected response of CAL. Other features, including regions of COL and LRNC are also delineated in the log(VoA) image.

IV. DISCUSSION

The results presented herein demonstrate that the outcome metric calculated as the log(VoA) better discriminates carotid plaque features that confer risk for stroke than ARFI PD. Further, the results suggest that by incorporating both CC and SNR, which are, respectively, related to the displacement and echogenicity of plaque components, log(VoA) achieves improved delineation of plaque composition and structure over analysis of CC or SNR alone.

Variations in CC may be caused by mechanical property differences among plaque components that yield diverse viscoelastic recoveries after the ARFI excitation. For example, IPH scatterers may exhibit no or very slow elastic recovery after the ARFI excitation. Thus, IPH scatterers may remain in motion after scatterers in the other plaque components have recovered, resulting in less correlated signal from regions of IPH than from other plaque regions. In regard to SNR, more highly echogenic plaque features, such as CAL deposits, have lower jitter magnitude, and thereby lower log(VoA), than plaque components that are less echogenic.

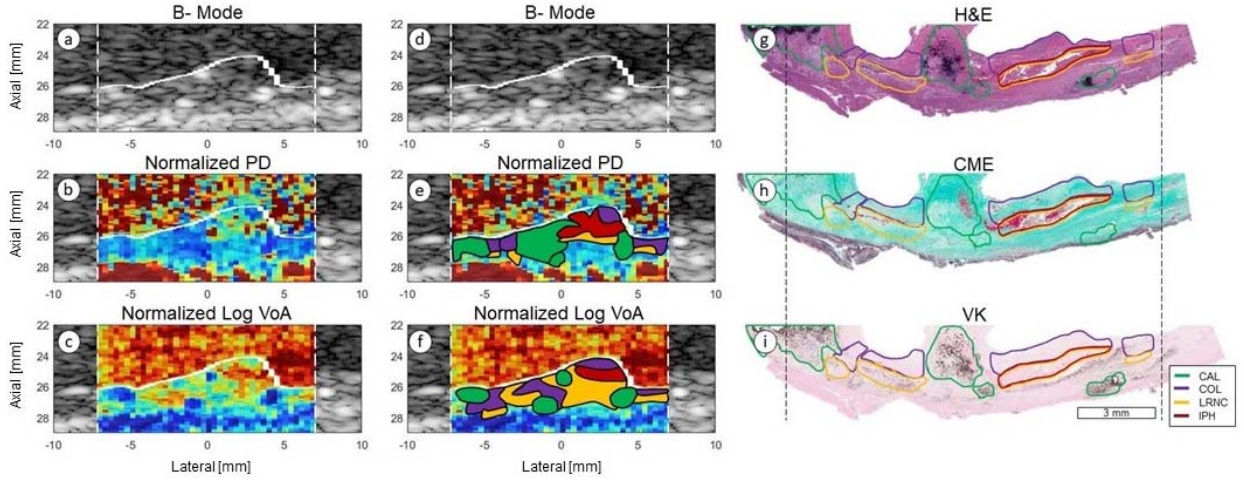

Fig. 9. Carotid ARFI images with matched histology from a 53-year-old symptomatic female. B-mode, normalized ARFI PD image, and normalized ARFI log(VoA) image, (a)–(c) without and (d)–(f) with component segmentations. Histological results of (g) H&E, (h) CME, and (i) VK stains, confirming the presence of CAL, COL, LRNC, and IPH plaque features. Features are denoted by color as CAL (green), COL (purple), LRNC (yellow), and IPH (red).

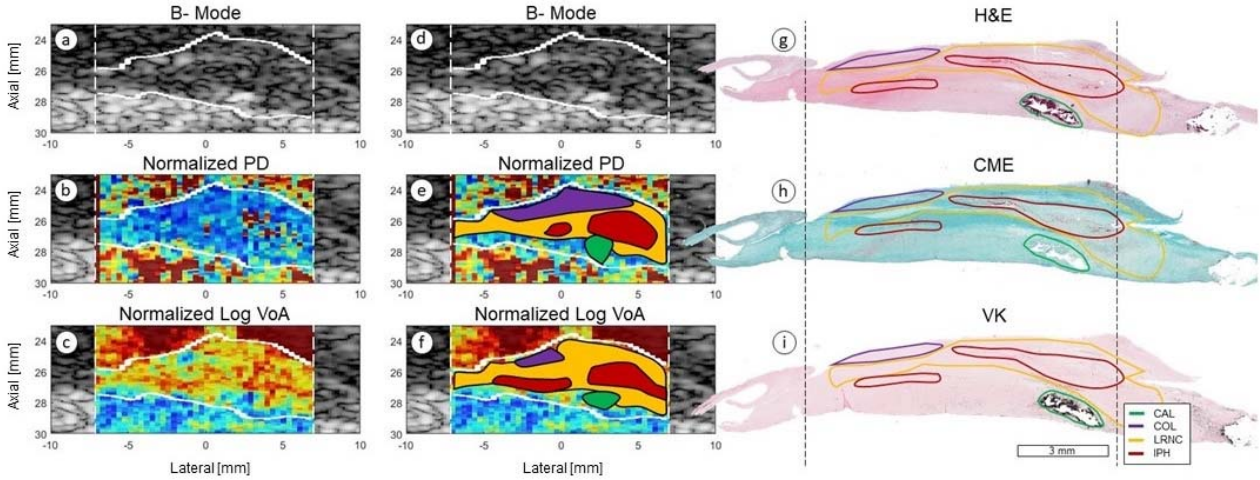

Fig. 10. Carotid ARFI images with matched histology from a 59-year-old symptomatic male. B-mode, normalized ARFI PD image, and normalized ARFI log(VoA) image, (a)–(c) without and (d)–(f) with component segmentations. Histological results of (g) H&E, (h) CME, and (i) VK stains, confirming the presence of CAL, COL, LRNC, and IPH plaque features. Features are denoted by color as CAL (green), COL (purple), LRNC (yellow), and IPH (red).

Plaque feature delineation performance by log(VoA) and by parameters derived from CC alone and SNR alone is compared by analyzing CNR in Tables I–III and parametric value distributions in Figs. 6–8. As expected, CC-derived values in IPH are generally lower than those in LRNC, but CC alone does not differentiate CAL from COL. Applying high-pass filtering by using the time-derivative operation and calculating the variance (as is performed for log(VoA) calculation) subtly improves separation of plaque features by CC. Similarly, SNR values in CAL are higher than those in COL, but LRNC and IPH are not differentiated by SNR alone.

The potential for visually discriminating LRNC from IPH and COL from CAL using optimized parameters derived by CC alone or SNR alone is explored in Figs. 4 and 5. In Fig. 4, regions of high SNR in the normalized image correspond to focal CAL deposits, and in Fig. 5, a region of low CC in the normalized image corresponds to IPH. While IPH is indicated in the CC images, no other plaque features are readily discernable. Furthermore, while CAL deposits are obvious in the SNR images, no other plaque features are apparent. Taken together, by visual inspection and CNR comparison, the evaluated data suggest that by incorporating both CC and SNR into a single metric, log(VoA) achieves more complete separation of plaque components than either CC or SNR alone.

In this work, log(VoA) was calculated as the decadic log of the variance of the second time-derivative of ARFI-induced displacement to exploit jitter magnitude. We note that other approaches to isolating jitter in displacement estimates are also possible, including frequency-domain filtering and mathematical calculations. Such alternative approaches are currently under investigation.

Previous studies have shown that ARFI is safe for carotid plaque imaging [41], [42]. Doherty *et al.* [43] showed that the magnitude of von Mises stress associated with ARFI excitations in arterial plaques ($<$1.2 kPa) is two orders of magnitude lower than the average arterial pressure stresses associated with ruptured (545.3 kPa) and unruptured (192.5 kPa) arterial plaque [41], [42].

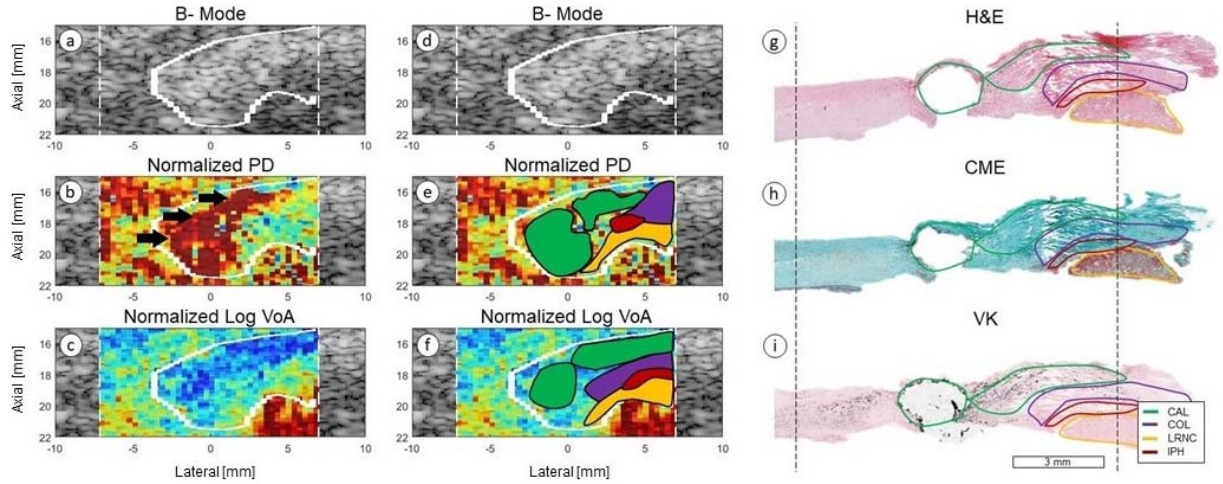

Fig. 11. Carotid ARFI images with matched histology from a 57-year-old symptomatic male. B-mode, normalized ARFI PD image, and normalized ARFI log(VoA) image, (a)–(c) without and (d)–(f) with component segmentations. Histological results of (g) H&E, (h) CME, and (i) VK stains, confirming the presence of CAL, COL, LRNC, and IPH plaque features. Features are denoted by color as CAL (green), COL (purple), LRNC (yellow), and IPH (red). Black arrows show PD misrepresentation of CAL due to artifacts caused by plaque interaction with the proximal wall.

The results reported herein agree with other work that histologically validated *in vivo*, noninvasive human carotid plaque component delineation by mechanical property. Like log(VoA), CUSI-detected lipid regions, which differentiated fibrous from (fibro)atheromatous plaques [14], [15]. CUSI's relevance to delineating IPH and CAL has not been demonstrated.

A limitation in the presented study design is that the examined *in vivo* human carotid plaque data were originally acquired for the purpose of evaluating ARFI PD. As a result, all acquisitions were gated to diastole, and the tracking ensemble time was limited to 5 ms. Therefore, it was not possible to thoroughly evaluate the impact of different degrees of arterial pressure/distention on log(VoA), and times longer than 5 ms after the ARFI excitation could not be examined. Future work will explore these variables.

A second limitation was the unequal number of plaque component examples, as indicated in Table IV, which impacted the pairwise Wilcoxon rank sum tests by diminishing the statistical power as the number of components become more unequal. More instances of statistically significant differences in parameter value and/or CNR may have been observed if the number of plaque component examples was equal.

Another limitation of this study is the impact of sample deformations on the spatial correlation between histology and ARFI images. Even though the plaque specimens were removed *en bloc* and immediately transferred to formalin solution, distortions still occurred. The primary causes of distortion were surgical extraction, fixation, and lack of pressurization, the latter two of which caused changes in tissue size. Despite these limitations, using μCT volumes of the extracted specimens enabled alignment of histology and ARFI imaging planes. Finally, an important consideration is the possibility of CAL deposits acting as local stress concentrators, which could confound ARFI-derived results.

While this work suggests that opportunities for log(VoA) to improve stroke risk prediction by delineating the structure and composition of carotid plaques are great, a potential challenge to optimal clinical application could be spatial resolution. For example, Czernuszewicz and Gallippi [37] previously demonstrated *in silico* that fibrous cap thickness resolution by ARFI PD is 0.2 mm—the upper limit on the critical fibrous cap thickness for predicting rupture [44]—when a 12-MHz center frequency is used. While the contrast mechanisms in ARFI PD and log(VoA) images differ, the prior work supports that higher center frequencies could improve feature size resolution by log(VoA). However, increasing the center frequency will decrease jitter magnitude, which could degrade log(VoA) feature discrimination if CC and SNR are rendered less impactful on the overall jitter value. Increasing the center frequency will also reduce penetration depth. Czernuszewicz and Gallippi [37] further demonstrated that decreasing the displacement tracking kernel length improves fibrous cap thickness resolution by ARFI PD. In log(VoA) estimation (2), decreasing the kernel length will increase jitter magnitude and, like increasing center frequency, could disrupt the influence of CC and SNR on the log(VoA) outcome parameter. Ultimately, identifying log(VoA) resolution limits and determining the ideal combination of imaging parameters for *in vivo* carotid plaque feature delineation will be important to realizing log(VoA)'s potential for improving stroke risk prediction clinically.

V. Conclusion

This work demonstrates the potential of the log(VoA) to improve *in vivo* carotid atherosclerotic plaque feature delineation relative to ARFI PD. Across all examined *in vivo* human carotid plaques, log (VoA) values were statistically significantly different between histologically confirmed regions of IPH and LRNC and between confirmed regions of COL and CAL, but this was not true for PD. Moreover, log (VoA) achieved higher CNR between IPH and LRNC, between COL and CAL, and between COL and LRNC than PD. Finally, the presented results demonstrate that although log (VoA) is influenced by both CC and SNR, evaluating CC alone or SNR alone does not differentiate IPH, LRNC, COL, and CAL as

well as log(VoA). Overall, these results support that log(VoA) is capable of describing the composition and structure of human carotid atherosclerotic plaque, *in vivo*, which is clinically useful for predicting stroke risk and facilitating medical management.

ACKNOWLEDGMENT

The authors would like to thank Siemens Healthcare, Ultrasound Division, Issaquah, WA, USA, for technical support.

REFERENCES

[1] E. J. Benjamin *et al.*, "Heart disease and stroke statistics—2019 update: A report from the american heart association," *Circulation*, vol. 1, no. 139, Mar. 2019.

[2] H. C. Stary, "Natural history and histological classification of atherosclerotic lesions: An update," *Arterioscler Thromb Vasc Biol.*, vol. 20, no. 5, pp. 1177–1178, 2000.

[3] P. K. Shah, "Mechanisms of plaque vulnerability and rupture," *J. Amer. Coll. Cardiol.*, vol. 41, pp. S15–S22, Feb. 2003.

[4] A. V. Finn, M. Nakano, J. Narula, F. D. Kolodgie, and R. Virmani, "Concept of vulnerable/unstable plaque," *Arterioscler Thromb Vasc Biol.*, vol. 30, no. 7, pp. 1282–1292, 2010.

[5] P. R. Moreno, "Vulnerable plaque: Definition, diagnosis, and treatment," *Cardiol. Clin.*, vol. 28, no. 1, pp. 1–30, 2010.

[6] J. L. Glover, P. J. Bendick, V. P. Jackson, G. J. Becker, R. S. Dilley, and R. W. Holden, "Duplex ultrasonography, digital subtraction angiography, and conventional angiography in assessing carotid atherosclerosis," *Arch. Surg.*, vol. 119, no. 6, pp. 664–669, 1984.

[7] P. Pignoli, E. Tremoli, A. Poli, P. Oreste, and R. Paoletti, "Intimal plus medial thickness of the arterial wall: A direct measurement with ultrasound imaging," *Circulation*, vol. 74, no. 6, pp. 1399–1406, 1986.

[8] J. T. Salonen and R. Salonen, "Ultrasound B-mode imaging in observational studies of atherosclerotic progression," *Circulation*, vol. 87, no. 3, pp. II56–II65, 1993.

[9] M. L. Bots, A. W. Hoes, P. J. Koudstaal, A. Hofman, and D. E. Grobbee, "Common carotid intima-media thickness and risk of stroke and myocardial infarction: The rotterdam study," *Circulation*, vol. 96, no. 5, pp. 1432–1437, 1997.

[10] M. W. Lorenz, H. S. Markus, M. L. Bots, M. Rosvall, and M. Sitzer, "Prediction of clinical cardiovascular events with carotid intima-media thickness: A systematic review and meta-analysis," *Circulation*, vol. 115, no. 4, pp. 459–467, 2007.

[11] V. A. Korshunov, S. M. Schwartz, and B. C. Berk, "Vascular remodeling: Hemodynamic and biochemical mechanisms underlying Glagov's phenomenon," *Arterioscler Thromb Vasc Biol.*, vol. 27, no. 8, pp. 1722–1728, 2007.

[12] L. Gerrit *et al.*, "Noninvasive imaging of the vulnerable atherosclerotic plaque," *Current Problems Cardiol.*, vol. 35, no. 11, pp. 556–591, 2010.

[13] G. Vegas-Sánchez-Ferrero *et al.*, "Gamma mixture classifier for plaque detection in intravascular ultrasonic images," *IEEE Trans. Ultrason., Ferroelectr., Freq. Control*, vol. 61, no. 1, pp. 44–61, Jan. 2014.

[14] H. H. G. Hansen, G. J. de Borst, M. L. Bots, F. L. Moll, G. Pasterkamp, and C. L. de Korte, "Compound ultrasound strain imaging for noninvasive detection of (fibro) atheromatous plaques: Histopathological validation in human carotid arteries," *JACC Cardiovascular Imag.*, vol. 9, no. 12, pp. 1466–1467, 2016.

[15] H. H. G. Hansen, G. J. de Borst, M. L. Bots, F. L. Moll, G. Pasterkamp, and C. L. de Korte, "Validation of noninvasive *in vivo* compound ultrasound strain imaging using histologic plaque vulnerability features," *Stroke*, vol. 47, no. 11, pp. 2770–2775, 2016.

[16] M.-H. Roy-Cardinal, F. Destrempes, G. Soulez, and G. Cloutier, "Assessment of carotid artery plaque components with machine learning classification using homodyned-K parametric maps and elastograms," *IEEE Trans. Ultrason., Ferroelect., Freq. Control*, to be published.

[17] X. Wang *et al.*, "Classification of symptomatic and asymptomatic patients with and without cognitive decline using non-invasive carotid plaque strain indices as biomarkers," *Ultrasound Med. Biol.*, vol. 42, no. 4, pp. 909–918, 2016.

[18] R. Nayak, G. Schifitto, and M. M. Doyley, "Visualizing angle-independent principal strains in the longitudinal view of the carotid artery: Phantom and *in vivo* evaluation," *Ultrasound Med. Biol.*, vol. 44, no. 7, pp. 1379–1391, 2018.

[19] R. X. Li *et al.*, "Pulse wave imaging in carotid artery stenosis human patients *in vivo*," *Ultrasound Med. Biol.*, vol. 45, no. 2, pp. 353–366, 2019.

[20] G. E. Trahey, M. L. Palmeri, R. C. Bentley, and K. R. Nightingale, "Acoustic radiation force impulse imaging of the mechanical properties of arteries: *In vivo* and *ex vivo* results," *Ultrasound Med. Biol.*, vol. 30, no. 9, pp. 1163–1171, 2004.

[21] C. Pislaru *et al.*, "*In vivo* vibroacoustography of large peripheral arteries," *Investigative Radiol.*, vol. 43, no. 4, p. 243, 2008.

[22] J. J. Dahl, D. M. Dumont, J. D. Allen, E. M. Miller, and G. E. Trahey, "Acoustic radiation force impulse imaging for noninvasive characterization of carotid artery atherosclerotic plaques: A feasibility study," *Ultrasound Med. Biol.*, vol. 35, no. 5, pp. 707–716, May 2009.

[23] D. M. Dumont, R. H. Behler, T. C. Nichols, E. P. Merricks, and C. M. Gallippi, "ARFI imaging for noninvasive material characterization of atherosclerosis," *Ultrasound Med. Biol.*, vol. 32, no. 11, pp. 1703–1711, Nov. 2006.

[24] R. H. Behler, T. C. Nichols, H. Zhu, E. P. Merricks, and C. M. Gallippi, "ARFI imaging for noninvasive material characterization of atherosclerosis part II: Toward *in vivo* characterization," *Ultrasound Med. Biol.*, vol. 35, no. 2, pp. 278–295, 2009.

[25] M. Couade *et al.*, "Quantitative assessment of arterial wall biomechanical properties using shear wave imaging," *Ultrasound Med. Biol.*, vol. 36, pp. 1662–1676, Oct. 2010.

[26] J. D. Allen, K. L. Ham, D. M. Dumont, B. Sileshi, G. E. Trahey, and J. J. Dahl, "The development and potential of acoustic radiation force impulse (ARFI) imaging for carotid artery plaque characterization," *Vascular Med.*, vol. 16, no. 4, pp. 302–311, 2011.

[27] D. M. Dumont, J. R. Doherty, and G. E. Trahey, "Noninvasive assessment of wall-shear rate and vascular elasticity using combined ARFI/SWEI/spectral Doppler imaging system," *Ultrason. Imag.*, vol. 33, no. 3, pp. 165–188, Jul. 2011.

[28] M. Bernal, I. Nenadic, M. W. Urban, and J. F. Greenleaf, "Material property estimation for tubes and arteries using ultrasound radiation force and analysis of propagating modes," *J. Acoust. Soc. Amer.*, vol. 129, no. 3, pp. 1344–1354, Mar. 2011.

[29] K. V. Ramnarine, J. W. Garrard, B. Kanber, S. Nduwayo, T. C. Hartshorne, and T. G. Robinson, "Shear wave elastography imaging of carotid plaques: Feasible, reproducible and of clinical potential," *Cardiovascular Ultrasound*, vol. 12, p. 49, Dec. 2014.

[30] K. Nightingale, M. S. Soo, R. Nightingale, and G. Trahey, "Acoustic radiation force impulse imaging: *In vivo* demonstration of clinical feasibility," *Ultrasound Med. Biol.*, vol. 28, no. 2, pp. 227–235, 2002.

[31] R. H. Behler *et al.*, "Acoustic radiation force beam sequence performance for detection and material characterization of atherosclerotic plaques: Preclinical, *ex vivo* results," *IEEE Trans. Ultrason., Ferroelectr., Freq. Control*, vol. 60, no. 12, pp. 2471–2487, Dec. 2013.

[32] T. J. Czernuszewicz *et al.*, "Non-invasive *in vivo* characterization of human carotid plaques with acoustic radiation force impulse ultrasound: Comparison with histology after endarterectomy," *Ultrasound Med. Biol.*, vol. 41, no. 3, pp. 685–697, 2015.

[33] T. J. Czernuszewicz *et al.*, "Performance of acoustic radiation force impulse ultrasound imaging for carotid plaque characterization with histologic validation," *J. Vascular Surg.*, vol. 66, no. 6, pp. 1749–1757.e3, 2017.

[34] A. Gupta, H. Baradaran, and A. D. Schweitzer, "Carotid plaque MRI and stroke risk: A systematic review and meta-analysis," *J. Vascular Surg.*, vol. 59, no. 4, p. 1175, Apr. 2014.

[35] L. J. Shaw, J. Narula, and Y. Chandrashekhar, "The never-ending story on coronary calcium: Is it predictive, punitive, or protective?" *J. Amer. College Cardiol.*, vol. 65, no. 13, pp. 1283–1285, Apr. 2015.

[36] G. F. Pinton, J. J. Dahl, and G. E. Trahey, "Rapid tracking of small displacements with ultrasound," *IEEE Trans. Ultrason., Ferroelectr., Freq. Control*, vol. 53, no. 6, pp. 1103–1117, Jun. 2006.

[37] T. J. Czernuszewicz and C. M. Gallippi, "On the feasibility of quantifying fibrous cap thickness with acoustic radiation force impulse (ARFI) ultrasound," *IEEE Trans. Ultrason., Ferroelectr., Freq. Control*, vol. 63, no. 9, pp. 1262–1275, Sep. 2016.

[38] W. F. Walker and G. E. Trahey, "A fundamental limit on delay estimation using partially correlated speckle signals," *IEEE Trans. Ultrason., Ferroelectr., Freq. Control*, vol. 42, no. 2, pp. 301–308, Mar. 1995.

[39] S. Lloyd, "Least squares quantization in PCM," *IEEE Trans. Inf. Theory*, vol. 28, no. 2, pp. 129–137, Mar. 2006.

[40] G. C. Cheng, H. M. Loree, R. D. Kamm, M. C. Fishbein, and R. T. Lee, "Distribution of circumferential stress in ruptured and stable atherosclerotic lesions. A structural analysis with histopathological correlation," *Circulation*, vol. 87, no. 4, pp. 1179–1187, Apr. 1993.
[41] H. M. Loree, R. D. Kamm, R. G. Stringfellow, and R. T. Lee, "Effects of fibrous cap thickness on peak circumferential stress in model atherosclerotic vessels," *Circulation Res.*, vol. 71, no. 4, pp. 850–858, Oct. 1992.
[42] Z.-Y. Li *et al.*, "Stress analysis of carotid plaque rupture based on *in vivo* high resolution MRI," *J. Biomech.*, vol. 39, no. 14, pp. 2611–2622, 2006.
[43] J. R. Doherty, D. M. Dumont, G. E. Trahey, and M. L. Palmeri, "Acoustic radiation force impulse imaging of vulnerable plaques: A finite element method parametric analysis," *J. Biomech.*, vol. 46, no. 1, pp. 83–90, 2013.
[44] J. N. E. Redgrave, J. K. Lovett, P. J. Gallagher, and P. M. Rothwell, "Histological assessment of 526 symptomatic carotid plaques in relation to the nature and timing of ischemic symptoms: The Oxford plaque study," *Circulation*, vol. 113, no. 19, pp. 2320–2328, May 2006.

Gabriela Torres (S'11) received the B.S. degree in electrical engineering from Pontificia Universidad Catolica del Peru, Lima, Peru, in 2015. She is currently pursuing the Ph.D. degree with the Joint Department of Biomedical Engineering, University of North Carolina at Chapel Hill, Chapel Hill, NC, USA, and the North Carolina State University, Raleigh, NC, USA.

Her current research interests include acoustic radiation force imaging methods and cardiovascular elasticity imaging.

Tomasz J. Czernuszewicz received the B.S. degree in biomedical engineering from Marquette University, Milwaukee, WI, USA, in 2007, and the Ph.D. degree from the Joint Department of Biomedical Engineering, University of North Carolina at Chapel Hill, Chapel Hill, NC, USA, and the North Carolina State University, Raleigh, NC, USA, in 2016.

He is currently the Chief Technology Officer at Sonovol Inc., Durham, NC, USA. His research interests include intravascular ultrasound and radiation force imaging methods.

Jonathon W. Homeister received B.A. degrees in biology and chemistry from Hope College, Holland, MI, USA, and the M.D. and Ph.D. (pharmacology) degrees from the University of Michigan, Ann Arbor, MI, USA, in 1993.

He did residency training in anatomic pathology at the University of Michigan Hospitals and is a Diplomat of the American Board of Pathology. He is currently an Associate Professor with the Department of Pathology and Laboratory Medicine, and a member with the McAllister Heart Institute, University of North Carolina at Chapel Hill, Chapel Hill, NC, USA. His research interests include the glycobiology inherent to leukocyte trafficking and lymphocyte homing and differentiation, particularly with respect to the pathogenesis of cardiovascular diseases, including atherosclerosis.

Melissa C. Caughey received the B.S. degree in biological sciences from North Carolina State University, Raleigh, NC, USA, in 1998, the M.P.H. degree from Emory University, Atlanta, GA, USA, and the Ph.D. degree from the University of North Carolina at Chapel Hill, Chapel Hill, NC, USA, with a focus on epidemiology.

She is currently an Instructor with the University of North Carolina School of Medicine, Chapel Hill, NC, USA. Her research interests include medical imaging biomarkers, biostatistical analysis, and the development of medical imaging technologies.

Benjamin Y. Huang received the M.D. degree from Duke University, Durham, NC, USA.

He completed his residency in diagnostic radiology from University of North Carolina at Chapel Hill (UNC), Chapel Hill, NC, USA, where he served as a Co-Chief Resident and completed a fellowship in neuroradiology. He has also trained in head and neck imaging at Emory University, Atlanta, GA, USA. He is board-certified in diagnostic radiology. He is currently a Clinical Associate Professor of radiology and the Neuroradiology Program Director with UNC.

Ellie R. Lee received the M.D. degree from Emory University School, Atlanta, GA, USA, in 1996.

She subsequently completed her residency in diagnostic radiology with the Duke University Medical Center, Durham, NC, USA, where she completed a fellowship in abdominal imaging. She is currently an Associate Professor of radiology with a focus on abdominal imaging with the University of North Carolina at Chapel Hill, Chapel Hill, NC, USA. Her research interest includes abdominal ultrasound imaging.

Carlos A. Zamora received the M.D. degree from Universidad de San Carlos, Guatemala City, Guatemala, and the Ph.D. degree in medical sciences from Kobe University, Kobe, Japan.

He completed his residency in diagnostic radiology and a two-year fellowship in neuroradiology at John Hopkins University Hospital, Baltimore, MD, USA. He is board-certified in diagnostic radiology and neuroradiology. He is currently a Clinical Assistant Professor of radiology with the University of North Carolina at Chapel Hill, Chapel Hill, NC, USA.

Mark A. Farber received the B.S. degree in chemical engineering from Cornell University, Ithaca, NY, USA, and the M.D. degree from Tulane University, New Orleans, LA, USA.

He completed his residency in general surgery from the University of North Carolina at Chapel Hill, Chapel Hill, NC, USA. He is currently a Professor of surgery, the Program Director of the Vascular Surgery Fellowship, and the Chief of the Vascular Surgery Division with the University of North Carolina at Chapel Hill. He is board-certified in vascular surgery. His research interests include endovascular surgery and endovascular repair of aortic disease.

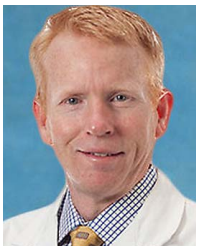

William A. Marston received the M.D. degree from the University of Virginia, Charlottesville, VA, USA, in 1988.

He completed his residency in general surgery in 1993, and completed a fellowship in vascular surgery at the University of North Carolina at Chapel Hill, Chapel Hill, NC, USA. He is board-certified in vascular surgery. He is currently a Professor of surgery and the Medical Director of the Wound Management Center with the University of North Carolina at Chapel Hill. His research interests include endovascular surgery, limb preservation, wound care, vein disorders, and dialysis access.

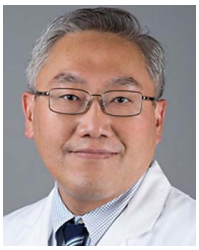

David Y. Huang received the M.D. degree from Duke University, Durham, NC, USA, in 1997.

He completed his residency in neurology at the Massachusetts General Hospital - Harvard School, Boston, MA, USA, in 2001, and a fellowship in stroke and neurologic critical care at the same institutions in 2002. He is board-certified in neurology with a subspecialty certification in vascular neurology, American Board of Psychiatry and Neurology. He is currently a Professor and the Chief of the Stroke and Vascular Neurology Division with the University of North Carolina at Chapel Hill, Chapel Hill, NC, USA.

Timothy C. Nichols received the B.S. degree from Stanford University, Stanford, CA, USA, in 1974, and the M.D. degree from the Medical College of Virginia, Richmond, VA, USA, in 1978.

He trained as an Internist, a Cardiologist, and a Researcher in atherosclerosis, thrombosis, and hemostasis. He is currently a Professor of medicine and pathology and laboratory medicine with the University of North Carolina at Chapel Hill, Chapel Hill, NC, USA, and is the Director of the Francis Owen Blood Research Laboratory. His research focuses on atherosclerosis in familial hypercholeterolemi pigs and inherited bleeding disorders in hemophilic and von Willebrand disease dogs, all of which are produced and maintained at the FOBRL.

Caterina M. Gallippi (M'98) received the B.S.E. degree in electrical engineering and the certificate in engineering biology from Princeton University, Princeton, NJ, USA, in 1998, and the Ph.D. degree in biomedical engineering from Duke University, Durham, NC, USA, in 2003, with a focus on ultrasonic imaging.

She is currently an Associate Professor with the Joint Department of Biomedical Engineering, University of North Carolina at Chapel Hill, Chapel Hill, NC, USA, and North Carolina State University, Raleigh, NC, USA. Her research interests include radiation force imaging, adaptive signal filtering, multidimensional motion tracking, and magnetomotive ultrasound.